

## RESEARCH ARTICLE

# Rapid Fabrication of Cobalt/Cobalt Oxide Heterostructured Catalysts for Efficient Electrochemical Water Splitting

Colton Jones | Josue Pizano | John Tressel | Shaowei Chen 

Department of Chemistry and Biochemistry, University of California, Santa Cruz, California, USA

Correspondence: Shaowei Chen ([shaowei@ucsc.edu](mailto:shaowei@ucsc.edu))

Received: 20 October 2025 | Revised: 15 January 2026 | Accepted: 11 February 2026

Keywords: Co/CoO heterostructure | hydrogen evolution reaction | magnetic induction heating | oxygen evolution reaction | water splitting

## ABSTRACT

Metal/carbon-based nanocomposites have attracted significant interest for electrochemical water splitting due to their unique interfacial electronic structures, abundant active sites, and catalytic bifunctionality toward both hydrogen evolution reaction (HER) and oxygen evolution reaction (OER). Herein, Co/CoO-rGO composites consisting of Co/CoO heterostructured nanoparticles encapsulated within a graphitized carbon scaffold are produced via magnetic induction heating at controlled currents for 10 s with cobalt(II) nitrate and reduced graphene oxide (rGO) loaded on nickel foam and effectively catalyze both HER and OER in alkaline media. Among the series, the sample prepared at 400 A for 10 s exhibits the best performance, featuring an overpotential of  $-144$  mV for HER and  $+390$  mV for OER at  $10$  mA cm $^{-2}$  and  $50$  mA cm $^{-2}$ , respectively. The bifunctional activity can then be exploited for full water splitting, where a low cell voltage of  $1.61$  V is needed to generate a current density of  $10$  mA cm $^{-2}$ ,  $260$  mV better than that with commercial Pt/C and RuO $_2$ . The remarkable performance is attributed to the synergistic interaction between the Co and CoO domains, enhanced charge transfer at the heterojunction interface, and conductive carbon support. These results highlight the potential of Co/CoO-based nanocomposites as efficient and low-cost catalysts for overall water splitting and the scalability of the MIH technology.

## 1 | Introduction

The ongoing energy crisis and environmental impacts of the combustion of fossil fuels has compelled researchers to explore clean and renewable alternatives [1–3]. Electrochemical water splitting is a viable response to current energy demands to produce hydrogen gas (H $_2$ ), a clean and efficient fuel source. However, the primary barrier for the widespread use of electrochemical water splitting is the substantial overpotentials needed to expedite reaction rates of both the hydrogen and oxygen evolution reactions (HER and OER). Catalysts are needed to reduce the substantial overpotentials and often contain precious metals, which are typically Pt for HER and IrO $_2$  and RuO $_2$  for OER [4]. The use of these precious metals further drive green hydrogen production away from commercialization as the unaffordable

cost and scarcity of noble metals makes large-scale utilization of electrochemical water splitting not economically viable [5–7]. Cobalt-based materials are promising earth-abundant candidates as bifunctional water-splitting electrocatalysts due to their accessible multiple oxidation states and favorable electronic structures [8–11]. In particular, Co/CoO heterostructures have been found to simultaneously provide metallic Co sites with optimal hydrogen adsorption for HER and cobalt oxide domains that transform into CoOOH as highly active OER centers [12]. However, these heterostructures typically suffer from limited intrinsic conductivity and nanoparticle aggregation, which hinder charge transport and active-site utilization. Coupling Co/CoO with conductive carbon supports such as reduced graphene oxide (rGO) can mitigate these issues by preventing aggregation, enhancing electron transport, and enabling strong interfacial electronic coupling.

Designing Co/CoO-carbon heterostructures that are both catalytically efficient and rapidly synthesized therefore remains an important challenge for practical water electrolysis.

The most common means of synthesizing these heterostructure composites is through thermal methods that are both time- and energy-intensive. Magnetic induction heating (MIH) has recently emerged as an efficient method for ultrafast preparation of a wide range of novel materials [13]. MIH utilizes the Joule heating effect to rapidly heat samples to over 1000°C in seconds. This rapid cooling rate, up to 200°C s<sup>-1</sup>, is markedly faster than that (<10°C min<sup>-1</sup>) of traditional heating techniques, which can take hours or even days to prepare a sample. The rapid heating of MIH can also be coupled with rapid cooling, which promotes the formation of metastable or nonequilibrium structures that can greatly improve catalytic efficiency. Indeed, MIH has recently been used to create remarkable catalysts for various applications, such as MoS<sub>x</sub> composites for HER [14], FeNi spinel oxides for OER [15], and Ru-RuO<sub>2</sub> heterostructures for full water-splitting applications [8].

Herein, nickel foam (NF)-supported Co/CoO heterostructured composites were prepared by using the conductive and magnetic NF as the heating substrate for MIH, with cobalt(II) nitrate and rGO as the precursors. The inclusion of rGO in the precursor served two purposes. The surface of rGO was rich with nucleation sites for nanoparticle formation and the dielectric character of the planar nanomaterial allowed for secondary oscillations to occur that enhanced eddy current generation on the surface of the NF, thus enhancing the heating rate [16–18]. The Co precursor on the surface of the NF underwent a disproportionate reaction during MIH treatment, where the readily formed CoO was partially reduced to form Co/CoO heterostructures as a result of carbothermal reduction by the rGO substrate [19]. Among the series, the sample prepared at 400 A for 10 s (Co/CoO-rGO-400) exhibited the best performance toward both HER and OER in alkaline media, featuring an HER overpotential at 10 mA cm<sup>-2</sup> ( $\eta_{\text{HER},10}$ ) of -144 mV and OER overpotential at 50 mA cm<sup>-2</sup> ( $\eta_{\text{OER},50}$ ) of +390 mV. The samples also demonstrated exceptional stability at operational voltages for an extended period of time. When the electrodes were used as bifunctional catalysts for full water splitting, a low cell voltage ( $E_{10}$ ) of only 1.61 V was required to produce a current density of 10 mA cm<sup>-2</sup>, in comparison to 1.87 V for commercial Pt/C and RuO<sub>2</sub>. This remarkable performance was ascribed to the formation of Co/CoO heterostructures that facilitated interfacial electron transfer and optimal binding of key reaction intermediates.

## 2 | Results and Discussion

### 2.1 | Structural Characterization

Experimentally, a solution containing rGO nanosheets and Co(NO<sub>3</sub>)<sub>2</sub> was sprayed onto NF pieces (Figure S1), which were then subject to MIH treatment at controlled currents ( $X = 200$ –600 A) for 10 s. The resulting samples were denoted as Co/CoO-rGO- $X$ . A control sample (rGO-400) was prepared in the same fashion at 400 A for 10 s but without the addition of Co(NO<sub>3</sub>)<sub>2</sub>. The details are included in the Experimental section. The sample structure was first examined by scanning electron microscopy

(SEM) measurements. From the SEM image in Figure S2a, it can be seen that after spray deposition of the Co(NO<sub>3</sub>)<sub>2</sub>-rGO ink followed by MIH treatment, the Co/CoO-rGO-400 composites exhibited a homogeneous coverage on the NF surface, and elemental mapping analysis based on energy-dispersive x-ray spectroscopy (EDS) clearly identified the elements of Co, O, and C that were distributed evenly across the sample (Figure S2b–d). In TEM measurements (Figures 1a and S3), Co/CoO-rGO-400 can be seen to consist of high-contrast nanoparticles distributed throughout the low-contrast nanosheet scaffold, ranging in size from 10 to 20 nm with an average 14.8 ± 0.6 nm (inset to Figure 1a). In the high-resolution TEM image (Figure 1b), the nanoparticles can be found to display crystalline domains in intimate contact, where several interplanar spacings can be resolved from the lattice fringes at 0.203 and 0.247 nm due to the cubic Co(111) (JCPDS File Card #15–0806) and cubic CoO (111) (JCPDS File Card #78–0431) planes, respectively. This confirms the formation of Co/CoO heterojunctions in the sample. Indeed, in EDS-based elemental mapping measurements (Figure 1c), it can be seen that Co and O are mostly confined within the nanoparticulates that are distributed rather evenly across the C matrix.

Further structural insights were obtained from x-ray photoelectron spectroscopy (XPS) measurements. From the survey spectra in Figure S4a, the C 1s, O 1s, and Co 2p electrons can be readily identified for Co/CoO-rGO-400 at ca. 285, 531, and 780 eV, respectively. Figure 2a shows the corresponding high-resolution scans of the Co 2p electrons. The Co/CoO-rGO-200 sample can be seen to possess a doublet at 781.3/796.8 eV due to the 2p<sub>3/2</sub>/2p<sub>1/2</sub> electrons of the Co<sup>2+</sup> species, along with a pair of satellite peaks at 785.9/802.5 eV [12, 20, 21]. Notably with increasing induction current (i.e., temperature), the binding energies of this doublet exhibited a slight red shift to 780.6/795.9 eV for Co/CoO-rGO-300, 780.3/795.7 eV for Co/CoO-rGO-400, 780.1/795.8 eV for Co/CoO-rGO-500, and 779.9/795.6 eV for Co/CoO-rGO-600. Meanwhile, a second doublet can also be resolved at ca. 778.2/794.7 eV for these samples, suggesting the emergence of metallic Co at induction currents above 300 A [15]. This is in good alignment with the results from TEM measurements where both CoO and metallic Co lattice fringes were observed (Figure 1b). In addition, the Co<sup>2+</sup> content can be seen to diminish from ca. 5.74 at% for Co/CoO-rGO-200 to 3.76 at% for Co/CoO-rGO-300, 2.95 at% for Co/CoO-rGO-400, 2.60 at% for Co/CoO-rGO-500, and 2.07 at% for Co/CoO-rGO-600, whereas the metallic Co content went from undetectable in Co/CoO-rGO-200 to 0.44 at% in Co/CoO-rGO-300, 0.62 at% in Co/CoO-rGO-400, 0.72 at% in Co/CoO-rGO-500, and 0.93 at% in Co/CoO-rGO-600 (Figure 2c and Table S1). This likely arose from an increase of graphitization of the rGO nanosheets and charge transfer from the carbon scaffold at high temperatures, resulting in partial reduction of CoO to form Co/CoO heterostructures [22]. In fact, in Raman measurements (Figure S5), the D and G bands of graphitic carbon can be resolved in all Co/CoO-rGO samples, and the intensity ratio ( $I_D/I_G$ ) diminishes with increasing MIH current. This is also consistent with the increasing content of the sp<sup>2</sup> C species, as manifested in the XPS C 1s spectra (Figure S4b and Table S2).

The high-resolution scans of the O 1s electrons are shown in Figure 2b. One can see that the Co/CoO-rGO composites all possess a noticeable peak (green color) at ca. 530.1 eV (along

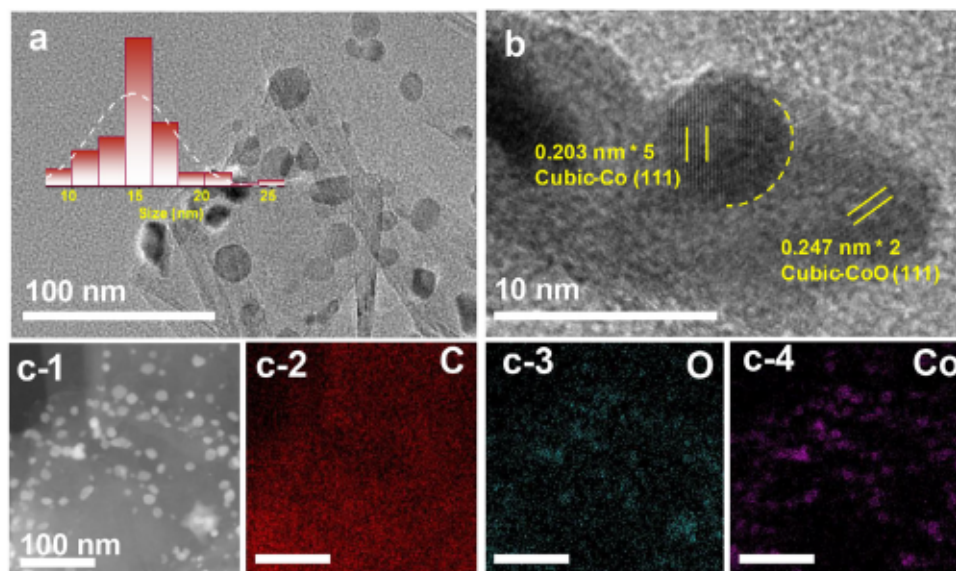


**FIGURE 1** | (a) Representative TEM image of Co/CoO-rGO-400. Inset is the corresponding nanoparticle size histogram. (b) HRTEM image of Co/CoO-rGO-400. (c-1) HAADF-STEM image of Co/CoO-rGO-400 and the corresponding elemental maps of (c-2) C, (c-3) O, and (c-4) Co.

with C–O at ca. 531.7 eV and C=O at ca. 533.4 eV), due to metal-O [15]. Additionally, the content decreases from 4.24 at% in Co/CoO-rGO-200 to 2.31 at% in Co/CoO-rGO-300, 2.10 at% in Co/CoO-rGO-400, 1.88 at% in Co/CoO-rGO-500, and 0.95 at% in Co/CoO-rGO-600 (Figure 2c and Table S3). This trend, alongside the decreasing Co<sup>2+</sup> content and the increasing metallic Co content among the sample series, suggests partial reduction of CoO to metallic Co particles and the formation of Co/CoO heterostructures in the carbon matrix (Figure 1b). In addition, from Tables S1 and S3, one can see that the atomic ratio of the Co<sup>2+</sup> and metal-O species can be estimated to be 1.35 for Co/CoO-rGO-200, 1.63 for Co/CoO-rGO-300, 1.40 for Co/CoO-rGO-400, 1.38 for Co/CoO-rGO-500, and 2.18 for Co/CoO-rGO-600, in line with the stoichiometry of CoO with increasing oxygen deficiency in the sample series. This was further corroborated by Raman measurements. From Figure 2d, one can see that the  $E_g$ ,  $T_{2g}$ , and  $A_{1g}$  vibrations of CoO can be resolved at ca. 489, 540, and 690 cm<sup>-1</sup>, respectively, and the peak intensity diminishes from Co/CoO-rGO-200 to Co/CoO-rGO-600 [23]. Taken together, these results confirm the formation of Co/CoO heterostructures in the samples due to partial reduction of CoO embedded within the carbon matrix.

In summary, these characterizations suggest that the formation of Co/CoO heterophased nanoparticles under MIH arose from the interplay between thermodynamically favorable carbothermal reduction and kinetic limitations imposed by ultrafast heating and cooling. During MIH, localized Joule heating at the rGO–Ni foam interface drove partial reduction of CoO to metallic Co by the carbon scaffold, while the short heating duration (10 s) and rapid quenching prevented full phase equilibration. This resulted in kinetically stabilized Co/CoO heterostructures within individual nanoparticles, with metallic Co domains preferentially forming at carbon–oxide interfaces. By increasing the MIH current from 200 to 600 A, the metallic Co fraction increased progressively, demonstrating that the Co/CoO phase composition and heterointerface density can be systematically tuned through the MIH parameters.

## 2.2 | Electrocatalytic Activity

### 2.2.1 | Hydrogen Evolution Reaction

The HER and OER electrocatalytic activities of the Co/CoO-rGO samples were then evaluated and compared in 1 M KOH (pH = 14). From the HER polarization curves in Figure 3a, one can see that in comparison to the minimal activity of pristine NF and rGO-400, the electrocatalytic performance was enhanced markedly with the Co/CoO-rGO composites, and Co/CoO-rGO-400 stood out as the best among the series, featuring an  $\eta_{\text{HER},10}$  of –144 mV, as compared to –188 mV for Co/CoO-rGO-500, –194 mV for Co/CoO-rGO-200, –202 mV for Co/CoO-rGO-300, and –226 mV for Co/CoO-rGO-600, although the performance remained subpar as compared to commercial Pt/C ( $\eta_{\text{HER},10} = -67$  mV). This suggests that the cobalt species, in particular, the formation of Co/CoO heterostructures, might play a critical role in the electrocatalytic activity.

The corresponding Tafel plots are shown in Figure 3b, where Co/CoO-rGO-400 featured a Tafel slope of 71.7 mV dec<sup>-1</sup>, markedly lower than others in the series, 93.4 mV dec<sup>-1</sup> for Co/CoO-rGO-200, 82.2 mV dec<sup>-1</sup> for Co/CoO-rGO-300, 73.8 mV dec<sup>-1</sup> for Co/CoO-rGO-500 and 120.1 mV dec<sup>-1</sup> for Co/CoO-rGO-600. This suggests that Co/CoO-rGO-400 possessed the most facile electron-transfer kinetics (the Tafel slope was much higher at 110.3 mV dec<sup>-1</sup> for NF and 112.7 mV dec<sup>-1</sup> for rGO-400, but only 32.2 mV dec<sup>-1</sup> for Pt/C). The Tafel slopes further emphasize the role of the Co/CoO heterostructures in facilitating electron transfer, which is corroborated in electrochemical impedance spectroscopy measurements. From the Nyquist plots in Figure 3c, Co/CoO-rGO-400 can be seen to display a charge transfer resistance ( $R_{ct}$ ) of 11.07  $\Omega$  at the overpotential of -100 mV, markedly lower than those of NF (28.06  $\Omega$ ) and rGO-400 (30.50  $\Omega$ ) but somewhat greater than that of Pt/C (5.11  $\Omega$ ), whereas the series resistance ( $R_s$ ) was consistent among the samples at ca. 1.0  $\Omega$ , confirming good electrical conductivity of the NF and rGO scaffolds.

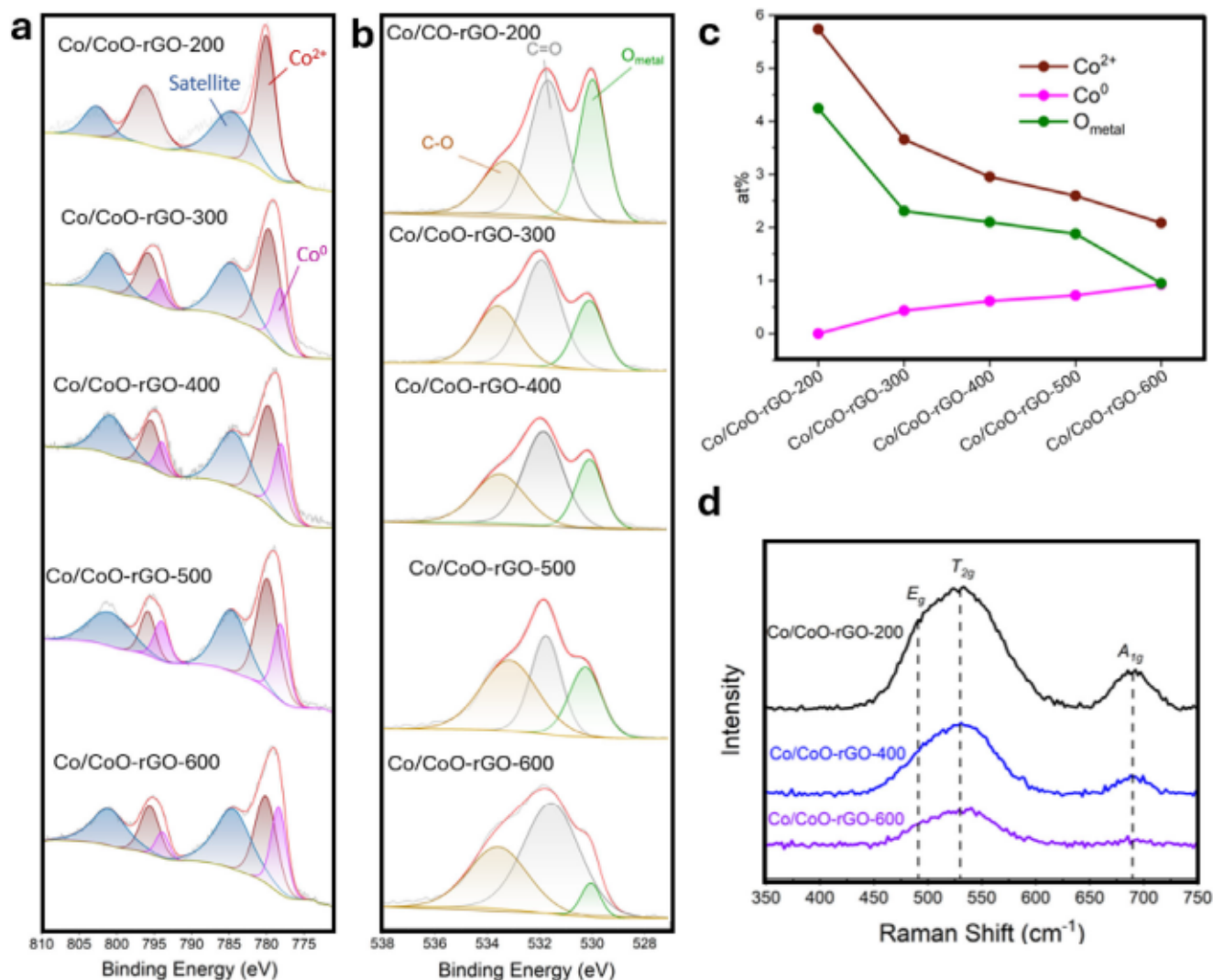


**FIGURE 2** | High-resolution XPS scans of the (a) Co 2p and (b) O 1s electrons of Co/CoO-rGO-200, Co/CoO-rGO-300, Co/CoO-rGO-400, Co/CoO-rGO-500, and Co/CoO-rGO-600. (c) Variation of the contents of different Co and O species. (d) Raman spectra of Co/CoO-rGO-200, Co/CoO-rGO-400, and Co/CoO-rGO-600.

The durability of Co/CoO-rGO-400 was also investigated. As seen in Figure 3d, Co/CoO-rGO-400 demonstrated exceptional stability after 2000 potential cycles, with a negative shift of  $\eta_{\text{HER},10}$  by only 7 mV. The operational stability of Co/CoO-rGO-400 was also demonstrated by maintaining a constant current density of 10 mA cm<sup>-2</sup> at the applied potential of -144 mV for 18 h (Figure 3d inset). Consistent results were obtained in structural characterization of Co/CoO-rGO-400 after 10 LSV cycles of HER (0 to -250 mV). XPS analysis reveals that the Co/CoO-rGO electrode underwent minimal chemical or structural change after HER operation in 1 M KOH. As shown in Figure S6, the Co 2p spectra before and after HER exhibited essentially unchanged Co<sup>0</sup> and Co<sup>2+</sup> components, with no emergence of high-valence Co<sup>3+</sup> features, indicating that the Co/CoO heterostructure was preserved under cathodic conditions. A slight increase in the metallic Co fraction was observed (from 0.62% to 0.68 at%), consistent with mild surface reduction of CoO under HER potentials. Likewise, the O 1s spectra show only minor variations associated with surface hydroxylation, while the lattice metal-O contribution remained largely intact. These results confirm

that HER imposed a chemically benign environment for the Co/CoO-rGO catalysts [24].

## 2.2.2 | Oxygen Evolution Reaction

The OER performance of the sample series was also investigated in 1 M KOH. From the OER polarization curves in Figure 4a, one can see that bare NF and rGO-400 again exhibited virtually no activity, whereas Co/CoO-rGO-400 featured a low overpotential ( $\eta_{\text{OER},50}$ ) of +390 mV to achieve a current density of 50 mA cm<sup>-2</sup>, as compared to +480 mV for Co/CoO-rGO-200, +420 mV for Co/CoO-rGO-300, +450 mV for Co/CoO-rGO-500, +490 mV for Co/CoO-rGO-600, and +470 mV for commercial RuO<sub>2</sub>. The corresponding Tafel plots are depicted in Figure 4b. It can be seen that Co/CoO-rGO-400 featured a slope of 58.2 mV dec<sup>-1</sup>, which is comparable to Co/CoO-rGO-300 with a slope of 59.3 mV dec<sup>-1</sup> as well as the commercial RuO<sub>2</sub> catalyst with a slope of 56.9 mV dec<sup>-1</sup>. The other samples in the series are noticeably higher: Co/CoO-rGO-200 (96.2 mV dec<sup>-1</sup>), Co/CoO-rGO-500 (76.1 mV

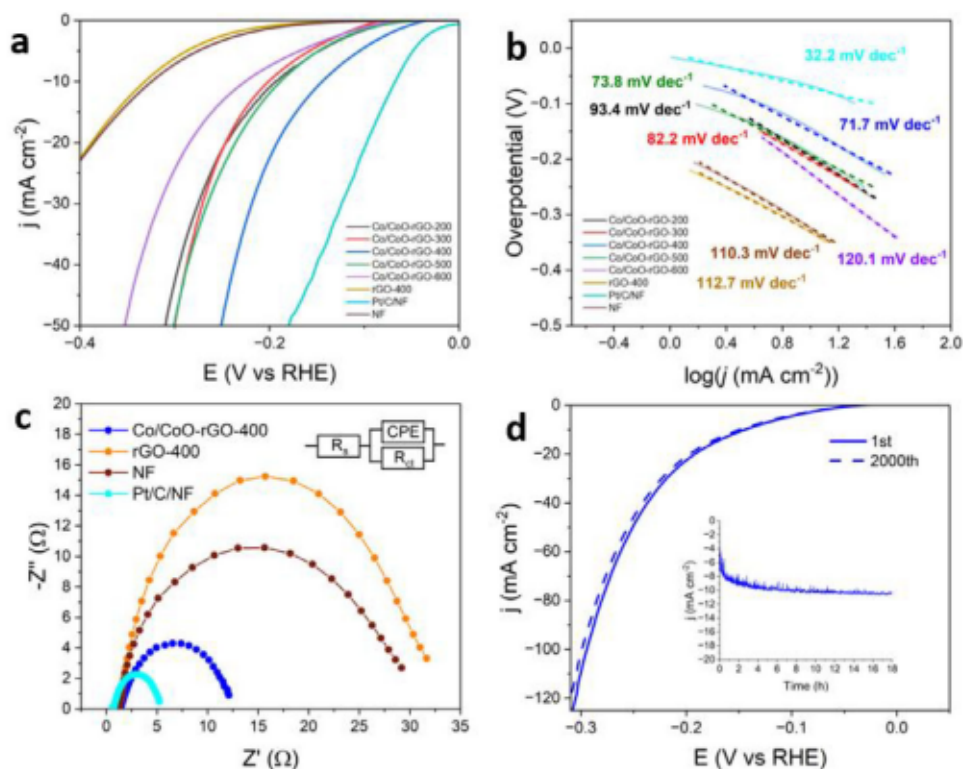


**FIGURE 3** | (a) HER polarization curves of the samples series and Pt/C on NF in 1 M KOH with a scan rate of  $10 \text{ mV sec}^{-1}$ . (b) Tafel plots of the samples series. (c) Nyquist plots of Co/CoO-rGO-400, rGO-400, bare NF, and Pt/C on NF at an overpotential of  $-100 \text{ mV}$ . Inset is the equivalent circuit, where  $R_s$  is the serial resistance,  $R_{ct}$  is the charge-transfer resistance, and CPE is the constant-phase element. (d) HER polarization curves of Co/CoO-rGO-400 before and after 2000 CV cycles. Inset is the  $i-t$  curve of Co/CoO-rGO-400 at an overpotential of  $-144 \text{ mV}$  in 1 M KOH.

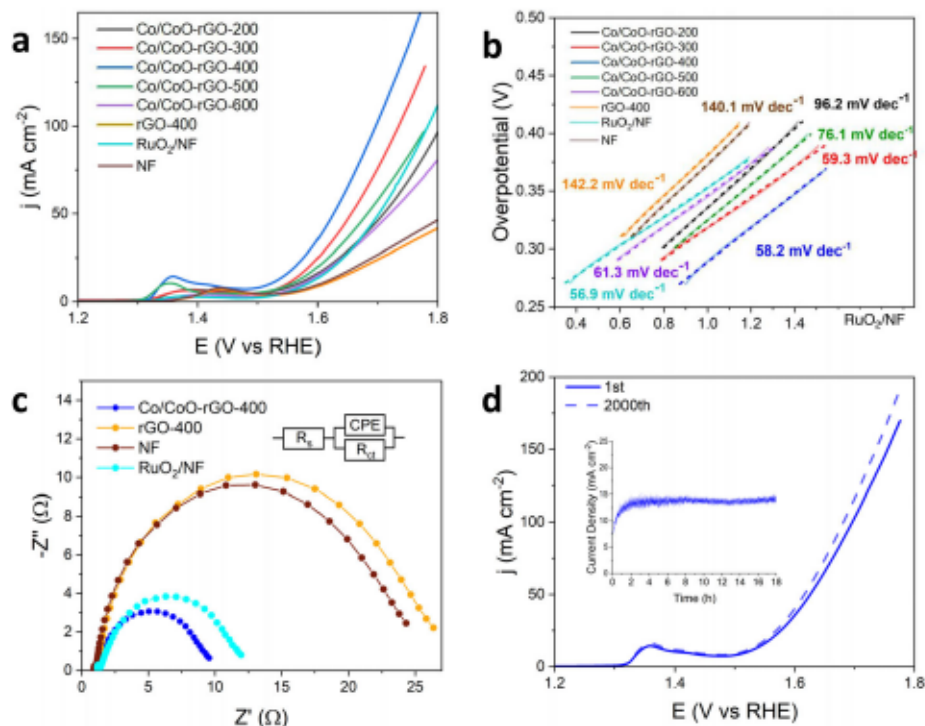


**FIGURE 4** | (a) OER polarization curves of the samples series and  $\text{RuO}_2$  on NF in 1 M KOH with a scan rate of  $10 \text{ mV sec}^{-1}$ . (b) Tafel plots of the samples series. (c) Nyquist plots of Co/CoO-rGO-400, rGO-400, NF, and  $\text{RuO}_2$  on NF at an overpotential of  $+400 \text{ mV}$ . Inset is the equivalent circuit, where  $R_s$  is the serial resistance,  $R_{ct}$  is the charge-transfer resistance, and CPE is the constant-phase element. (d) OER polarization curves of Co/CoO-rGO-400 before and after 2000 CV cycles. Inset is the  $i-t$  curve of Co/CoO-rGO-400 at an overpotential of  $+335 \text{ mV}$  in 1 M KOH.

$\text{dec}^{-1}$ ), Co/CoO-rGO-600 ( $73.7 \text{ mV dec}^{-1}$ ), rGO-NF ( $142.2 \text{ mV dec}^{-1}$ ), and NF ( $140.1 \text{ mV dec}^{-1}$ ). This suggests that Co/CoO-rGO-400 exhibited the most facile electron-transfer kinetics among the sample series in OER. In fact, from the Nyquist plots in Figure 4c acquired at the overpotential of +400 mV, Co/CoO-rGO-400 can be observed to possess an  $R_{ct}$  of  $8.60 \Omega$ , which is substantially lower than those of RuO<sub>2</sub> ( $11.12 \Omega$ ), NF ( $23.38 \Omega$ ), and rGO-400 ( $25.41 \Omega$ ). In addition, Co/CoO-rGO-400 exhibited remarkable stability, as manifested in the small positive shift of  $\eta_{\text{OER},50}$  by only 7 mV after 2000 potential cycles and good retention of the current density in chronoamperometric measurements at the overpotential of +335 mV for up to 18 h (Figure 4d and inset).

Furthermore, Co/CoO-rGO-400 exhibited the highest double-layer capacitance ( $C_{dl}$ ,  $25.3 \text{ mF cm}^{-2}$ ), in comparison to NF ( $2.2 \text{ mF cm}^{-2}$ ) and rGO-400 ( $1.8 \text{ mF cm}^{-2}$ ) alone (Figure S7), corresponding to an electrochemically active surface area (ECSA) of 872, 75.9, and  $62.1 \text{ cm}^2$ , respectively [25]. This means that incorporation of the Co/CoO heterostructures on rGO markedly increased the accessible electrochemical surface area by more than an order of magnitude relative to the individual components. This large enhancement indicates that the heterointerface between metallic Co, semiconducting CoO, and conductive rGO created a defect-rich, nanostructured surface with a high density of electrochemically addressable active sites. The substantially higher ECSA provided a quantitative basis for the markedly improved HER and OER activities of Co/CoO-rGO-400, as it enabled greater catalyst–electrolyte contact and more efficient utilization of catalytically active cobalt sites.

The enhanced OER activity of Co/CoO-rGO-400 was further explored by Raman spectroscopy and XPS measurements with samples collected after 10 scans of the OER polarization curves. From the Raman spectra presented in Figure S8a, it can be seen that Co/CoO-rGO-400 possessed new Raman peaks at 469, 511, 610, and  $671 \text{ cm}^{-1}$ , which actually corresponded to the  $E_g$ ,  $F_{2g}$ , and  $A_{1g}$  vibrational modes of a mixed valence spinel cobalt oxide species,  $\text{Co}_3\text{O}_4$ . This suggests the formation of  $\text{Co}^{3+}$  species, most likely due to the high electrode potentials of OER. This is further supported by XPS measurements of the Co 2p and O 1s electrons of Co/CoO-rGO-400. After OER polarization, deconvolution of the Co 2p spectrum (Figure S8b) yielded a primary doublet at  $779.10/794.97 \text{ eV}$ , suggesting the formation of  $\text{Co}^{3+}$  species, whereas the metallic  $\text{Co}^0$  peaks at  $778.19/794.91 \text{ eV}$  disappeared [26]. The resultant electron-deficient Co sites are optimal for OER because a unity occupancy of the  $E_g$  orbitals for the Co atoms can facilitate the coupling of \*OH groups, promote proton-coupled electron transfer, and enhance the chemisorption of \*OOH intermediates, thus lowering OER overpotentials and increasing O<sub>2</sub> production [12, 27–29]. The associated O 1s spectrum is shown in Figure S8c, and deconvolution yielded a peak at  $528.81 \text{ eV}$ , which can be ascribed to the formation of oxyhydroxide (OOH) species [30]. This suggests effective structural transformation of the heterostructured composites to CoOOH on the surface that has been known to be the actual active sites for OER electrocatalysis [12].

The superior bifunctional electrocatalytic performance of the Co/CoO-rGO-400 sample toward both HER and OER can be attributed to a finely tuned interplay between composition, electronic structure, and interfacial architecture. MIH at 400

A induced a partial reduction of CoO to metallic Co, yielding an optimal ratio of  $\text{Co}^0$  and  $\text{Co}^{2+}$  species that resulted in the formation of Co/CoO heterojunctions. It is likely that the Mott–Schottky characters facilitated interfacial electron transfer, as manifested in electrochemical impedance measurements [8, 31]. For HER, the presence of metallic cobalt provided active sites with favorable hydrogen adsorption energies, while for OER, the CoO domains promoted the generation of high-valence CoOOH intermediates essential for oxygen evolution [12]. The synergy at the Co/CoO interface enabled dynamic electron redistribution that modulated the binding energies of reaction intermediates, thereby improving catalytic efficiency for both reactions. These results are comparable/superior to those of relevant Co-based nanocomposites reported recently in the literature (Table S4). In addition to phase composition, the degree of graphitization of the rGO scaffold might also play a critical role. The MIH treatment at 400 A likely resulted in sufficient rGO graphitization to enhance electrical conductivity without over-reducing the cobalt oxide phase, ensuring strong electronic coupling between the nanoparticles and the carbon support. This conductive matrix promoted rapid charge transport, minimized kinetic losses, and ensured dispersion of the active Co-CoO domains. Indeed, electrochemical impedance spectroscopy measurements revealed that Co/CoO-rGO-400 exhibited the lowest charge transfer resistance among the sample series, while Tafel analysis indicated the most favorable reaction kinetics for both HER and OER. Furthermore, the sample possessed the highest double-layer capacitance, indicative of a large electrochemical surface area and high density of accessible active sites. Samples treated at lower induction currents (e.g., Co/CoO-rGO-200 and Co/CoO-rGO-300) lacked sufficient metallic cobalt content, while those treated at higher currents (e.g., Co/CoO-rGO-500 and Co/CoO-rGO-600) suffered from excessive reduction and diminishment of catalytically active CoO.

One may notice that although the Co/CoO-rGO-400 electrode exhibits bifunctional activity toward both HER and OER, the absolute overpotentials ( $\eta_{10} = -144 \text{ mV}$  for HER and  $\eta_{50} = +390 \text{ mV}$  for OER) remain moderate compared with noble-metal benchmarks. This behavior is mainly attributed to partial utilization of the internal Ni foam surface and the nonfully optimized Co/CoO phase composition under the present MIH conditions, as reflected by the moderate  $C_{dl}$  value ( $25.3 \text{ mF cm}^{-2}$ ). In addition, a fraction of the Co species was partially embedded within the rGO matrix, which limited the number of fully exposed active sites, and partial masking by H<sub>2</sub> or O<sub>2</sub> bubbles adhered on the porous electrode surface may further increase the apparent overpotentials at elevated currents, although this effect was expected to be secondary at low current densities used for  $\eta_{10}$  evaluation. Despite these limitations, the coexistence of metallic Co and CoO domains enabled efficient coupling of HER- and OER-relevant active sites within a single architecture, motivating further evaluation of Co/CoO-rGO-400 as a bifunctional electrode for full water-splitting configurations.

### 2.2.3 | Full Water Splitting

Motivated by the efficient bifunctional catalytic performance of Co/CoO-rGO-400, the full water-splitting capability of the sample was then investigated. A water-splitting electrolyzer was

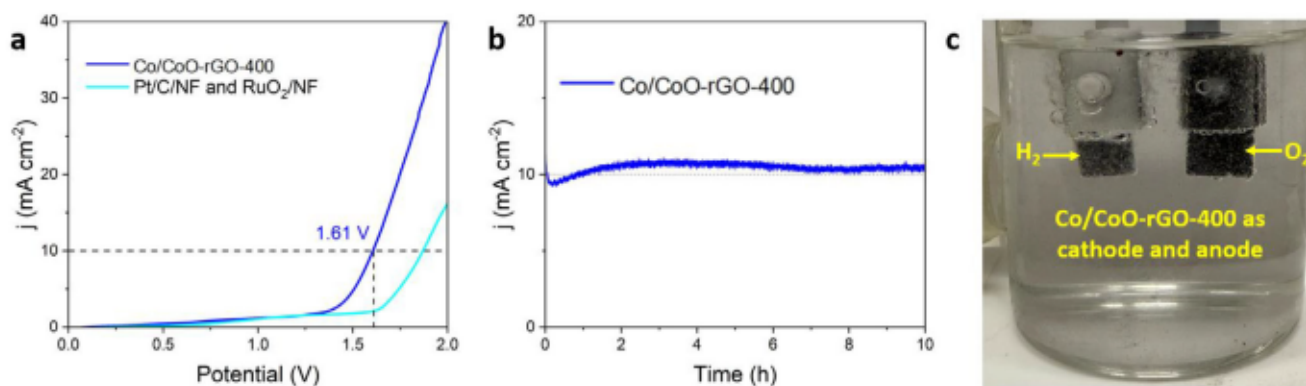


**FIGURE 5** | (a) Polarization curves of two-electrode systems with Co/CoO-rGO-400 couple and Pt/C/NF and RuO<sub>2</sub>/NF as electrodes in 1 M KOH for overall water splitting. (b) *i-t* curve of the Co/CoO-rGO-400-based electrolyzer at the applied voltage of 1.61 V in 1 M KOH. (c) Photograph of the evolution of H<sub>2</sub> and O<sub>2</sub> gases on Co/CoO-rGO-400 electrodes.

constructed by using the Co/CoO-rGO-400 electrode for both the cathode and anode catalyst in 1.0 M KOH. The Co/CoO-rGO-400 couple required an applied voltage ( $E_{10}$ ) of only 1.61 V to achieve a current density of 10 mA cm<sup>-2</sup>, as seen in Figure 5a. This outperformed a similar cell constructed with NF electrodes coated with commercial Pt/C at the cathode and RuO<sub>2</sub> at the anode, which required a higher applied voltage of 1.87 V [32]. Moreover, the long-term stability of the Co/CoO-rGO-400-based electrolyzer was also examined. It can be seen from Figure 5b that the electrolytic current (10 mA cm<sup>-2</sup>) remained virtually unchanged for 10 h at the applied voltage of 1.61 V. Generation of H<sub>2</sub> and O<sub>2</sub> gases can be readily observed on the electrode surfaces (Figure 5c) [33].

One may observe the discrepancy between the superior HER activity of Pt/C ( $\eta_{10} = -67$  mV) and the inferior overall water-splitting performance of the Pt/C||RuO<sub>2</sub> cell ( $E_{10} = 1.87$  V). This likely arose from the fact that the overall cell voltage was governed by the slower half-reaction, namely OER at the anode. While Pt/C provide nearly ideal HER kinetics, the RuO<sub>2</sub> electrode exhibited comparatively sluggish OER activity under the present loading and preparation conditions, as verified by its higher OER overpotential and charge-transfer resistance relative to Co/CoO-rGO-400 in the three-electrode configuration. Consequently, the OER overpotential at the RuO<sub>2</sub> anode dominated the full-cell voltage, offsetting the advantage of Pt at the cathode. In contrast, Co/CoO-rGO-400 simultaneously provided moderate HER activity and superior OER kinetics, enabling a more balanced bifunctional coupling and resulting in a significantly lower overall cell voltage ( $E_{10} = 1.61$  V). These results highlight that bifunctional kinetic matching between the cathode and anode may be more critical for minimizing overall water-splitting voltage than maximizing a single half-reaction alone, validating the advantage of the Co/CoO heterostructure for integrated water-splitting systems.

### 3 | Conclusion

In summary, Co/CoO heterostructured composites were prepared by rapid heating of NF coated with Co(NO<sub>3</sub>)<sub>2</sub> and rGO precursors using contactless MIH at controlled induction currents, where Co/CoO nanoparticles were dispersed onto the rGO nanosheet surface. The sample prepared at 400 A for 10 s, Co/CoO-rGO-400,

was found to exhibit the best bifunctional performance with an  $\eta_{\text{HER},10}$  of -144 mV and  $\eta_{\text{OER},50}$  of +390 mV. When Co/CoO-rGO-400 was used as the bifunctional catalysts for full water splitting, a low cell voltage of 1.61 V was required to achieve 10 mA cm<sup>-2</sup>, which outperformed a cell constructed using commercial Pt/C and RuO<sub>2</sub> by 260 mV. Co/CoO-rGO-400 also exhibited excellent durability. The enhanced activity and durability of the Co/CoO-rGO-400 electrode was ascribed to the Mott-Schottky character of the Co/CoO heterostructures, which afforded bifunctionality and enhanced electron transfer, and the rGO substrate enhanced electrical conductivity of the sample while also enhancing the MIH heating effect. Results of this study further highlight the capabilities of MIH, not only as a means of engineering unique materials, but also as a potential means of producing affordable high-performance materials at an industrial scale.

## 4 | Experimental Section

### 4.1 | Chemicals

Graphite powders (Spectrum Chemicals), NF (1-2 mm in thickness, 99.99% purity, SGS Certified-GDMS Tested, StonyLab), cobalt(II) nitrate hexahydrate (Co(NO<sub>3</sub>)<sub>2</sub>·6H<sub>2</sub>O, 99%, Acros), sulfuric acid (H<sub>2</sub>SO<sub>4</sub>, 98%, Fisher Chemicals), potassium permanganate (KMnO<sub>4</sub>, 99%, Fisher Chemicals), hydrogen peroxide (H<sub>2</sub>O<sub>2</sub>, 30%, Fisher Chemicals), hydrochloric acid (HCl, 37%, Fisher Chemicals), potassium hydroxide (KOH, Fisher Chemicals), platinum on graphitized carbon (Pt/C, 20 wt%, Sigma-Aldrich), and ruthenium (IV) oxide (RuO<sub>2</sub>, 99.9% trace metals basis, Sigma-Aldrich) were all used as received. Water was supplied by a Barnstead Nanopure water system (resistivity 18.3 MΩ cm).

### 4.2 | Synthesis of rGO

Graphene oxide (GO) was synthesized by a modified Hummers method [34]. In a typical experiment, graphite flakes (1 g) were transferred into a 250 mL round-bottom flask. 23 mL of concentrated H<sub>2</sub>SO<sub>4</sub> was added into the flask and the mixture was stirred at room temperature for 24 h before being heated in an oil bath at 40°C. 100 mg of NaNO<sub>3</sub> was added to the suspension

and allowed to dissolve in 5 min followed by the slow addition of 3 g of  $\text{KMnO}_4$  under magnetic stirring for 30 min, with the solution temperature kept below  $45^\circ\text{C}$ . The flask was removed from the oil bath and 140 mL of Nanopure water and 10 mL of 30%  $\text{H}_2\text{O}_2$  were added to the reaction vessel under magnetic stirring at room temperature for 5 min. The mixture was then centrifuged and washed with a 5% HCl solution twice, followed by rinsing with copious amounts of water. The final precipitate was dispersed in 100 mL of water under sonication for 30 min. Insoluble solids were removed by centrifugation at 3000 rpm for 5 min, and the brown supernatant (GO nanosheets) was collected and dried in an oven at  $70^\circ\text{C}$ , before being re-dispersed in water and hydrothermally reduced at  $150^\circ\text{C}$  for 24 h, yielding rGO nanosheets that were collected, rinsed with ethanol three times, and dried in an oven at  $70^\circ\text{C}$  for 12 h.

### 4.3 | Sample Preparation

NF pieces (1 cm  $\times$  1 cm) were sonicated for 10 min in acetone to remove any surface debris and immersed in 0.1 M HCl under sonication for 30 min to remove nickel oxides from the surface before being thoroughly rinsed with Nanopure water. A sprayable ink was prepared by dispersing 20 mg of the rGO nanosheets prepared above, 1 mmol of  $\text{Co}(\text{NO}_3)_2 \cdot 6\text{H}_2\text{O}$ , and 120  $\mu\text{L}$  of a 5% Nafion solution in 10 mL of isopropyl alcohol. The ink was then applied to the clean NF surface by spraying one side of the substrate ten times, allowing the NF to dry, and then repeating the spray deposition process on the other side. This process was repeated until the entire volume of the prepared ink was used, ensuring a thorough coverage of the  $\text{Co}(\text{NO}_3)_2$ -rGO mixture on the NF surface resulting in an approximate mass loading of 59  $\mu\text{g}$  of Co per  $\text{cm}^2$ . The spray apparatus and a prepared sample are shown in Figure S1.

After drying for 30 min under ambient conditions, the  $\text{Co}(\text{NO}_3)_2$ -rGO treated NF was sandwiched between two clean glass slides to prevent contamination, mounted on a fire block inside of a stoppered quartz tube and purged with high purity Ar gas for 20 min. The quartz tube was then set into a four-turn induction coil with a diameter of 5 cm, and MIH was carried out at a controlled current ( $X = 200\text{--}600$  A) for a heating time of 10 s before the sample was naturally cooled down to room temperature. The resulting samples were denoted as Co/CoO-rGO-X.

A control sample was also prepared in the same manner with rGO alone (without the addition of  $\text{Co}(\text{NO}_3)_2$ ) at 400 A for 10 s and denoted as rGO-400.

### 4.4 | Material Characterization

SEM measurements were conducted on a Thermo Scientific Apreo microscope at 10 kV. TEM measurements were carried out on a JOEL JEM 2100F microscope at 200 kV equipped with an Oxford instruments EDS attachment. XPS measurements were carried out with a Thermo Fisher K-alpha system, where the binding energy was calibrated against the C 1s binding energy. Raman measurements were conducted using a Horiba Jobin Yvon LabRAM ARAMIS automated scanning confocal Raman microscope under 532 nm excitation.

### 4.5 | Electrochemistry

Electrochemical studies were carried out with a CHI 700E electrochemical workstation in a three-electrode configuration. Electrochemical impedance and stability measurements were carried out with a Gamry Reference 600 instrument. A graphite rod was used as the counter electrode and a Hg/HgO in 1 M KOH as the reference electrode. The reference electrode was calibrated against a reversible hydrogen electrode (RHE) and all potentials in the present study were referenced to this RHE. Full water-splitting measurements were performed in a two-electrode configuration. The obtained NF samples were cut into 0.2 cm  $\times$  1.0 cm strips and held by a PTFE electrode holder with a total exposed surface area of 0.4  $\text{cm}^2$ . For comparison, commercial Pt/C and  $\text{RuO}_2$  samples were prepared at the same metal loading using the process reported above. No iR correction was applied.

### Supporting Information

Additional experimental data.

### Acknowledgments

The authors thank Drs. B. Yu and D. DuBois for the assistance of data acquisition. This work was supported by the National Science Foundation (CBET- 2522958). TEM, XPS, and Raman studies were conducted as part of a user project at the Molecular Foundry and National Center for Electron Microscopy of Lawrence Berkeley National Laboratory, which is supported the U.S. Department of Energy under contract No. DE-AC02-05CH11231.

### Conflicts of Interest

The authors declare no conflicts of interest.

### Data Availability Statement

The data that support the findings of this study are available on request from the corresponding author. The data are not publicly available due to privacy or ethical restrictions.

### References

1. H. B. Gray, "Powering the Planet with Solar Fuel," *Nature Chemistry* 1 (2009): 7–7, <https://doi.org/10.1038/nchem.141>.
2. N. S. Lewis, "Toward Cost-Effective Solar Energy Use," *Science* 315 (2007): 798–801, <https://doi.org/10.1126/science.1137014>.
3. J. A. Turner, "Sustainable Hydrogen Production," *Science* 305 (2004): 972–974, <https://doi.org/10.1126/science.1103197>.
4. H. J. Yan, C. G. Tian, L. Wang, et al., "Phosphorus-Modified Tungsten Nitride/Reduced Graphene Oxide as a High-Performance, Non-Noble-Metal Electrocatalyst for the Hydrogen Evolution Reaction," *Angewandte Chemie International Edition* 54 (2015): 6325–6329, <https://doi.org/10.1002/anie.201501419>.
5. J. J. Duan, S. Chen, A. Vasileff, and S. Z. Qiao, "Anion and Cation Modulation in Metal Compounds for Bifunctional Overall Water Splitting," *ACS Nano* 10 (2016): 8738–8745, <https://doi.org/10.1021/acs.nano.6b04252>.
6. B. J. Jiang, S. Z. Song, J. Q. Wang, et al., "Nitrogen-Doped Graphene Supported Pd@PdO Core-Shell Clusters for C-C Coupling Reactions," *Nano Research* 7 (2014): 1280–1290, <https://doi.org/10.1007/s12274-014-0492-1>.

7. N. Johnson, M. Liebreich, D. M. Kammen, P. Ekins, R. McKenna, and I. Staffell, "Realistic Roles for Hydrogen in the Future Energy Transition," *Nature Reviews Clean Technology* 1 (2025): 351–371.
8. D. J. Pan, B. Z. Yu, J. Tressel, et al., "Rapid Synthesis of Carbon-Supported Ru-RuO<sub>2</sub> Heterostructures for Efficient Electrochemical Water Splitting," *Advanced Science* 12 (2025): 2414534, <https://doi.org/10.1002/advs.202414534>.
9. Y. Jiang, Y. P. Deng, R. L. Liang, et al., "d-Orbital Steered Active Sites through Ligand Editing on Heterometal Imidazole Frameworks for Rechargeable Zinc-air Battery," *Nature Communications* 11 (2020): 5858, <https://doi.org/10.1038/s41467-020-19709-6>.
10. Z. K. Yang, C. M. Zhao, Y. T. Qu, et al., "Trifunctional Self-Supporting Cobalt-Embedded Carbon Nanotube Films for ORR, OER, and HER Triggered by Solid Diffusion from Bulk Metal," *Advanced Materials* 31 (2019): 1808043, <https://doi.org/10.1002/adma.201808043>.
11. P. Yu, L. Wang, F. F. Sun, et al., "Co Nanoislands Rooted on Co-N-C Nanosheets as Efficient Oxygen Electrocatalyst for Zn-Air Batteries," *Advanced Materials* 31 (2019): 1901666, <https://doi.org/10.1002/adma.201901666>.
12. Q. M. Liu, S. McNair, F. Nichols, et al., "Ultrafast Synthesis of Cobalt/Carbon Nanocomposites by Magnetic Induction Heating for Oxygen Evolution Reaction," *Advanced Sensor and Energy Materials* 2 (2023): 100046, <https://doi.org/10.1016/j.asems.2023.100046>.
13. Q. M. Liu and S. W. Chen, "Ultrafast Synthesis of Electrocatalysts," *Trends in Chemistry* 4 (2022): 918–934, <https://doi.org/10.1016/j.trechm.2022.07.004>.
14. Q. M. Liu, F. Nichols, A. Bhuller, et al., "Ultrafast Synthesis of Amorphous Molybdenum Sulfide by Magnetic Induction Heating for Hydrogen Evolution Reaction," *Applied Catalysis B: Environmental* 342 (2024): 123399, <https://doi.org/10.1016/j.apcatb.2023.123399>.
15. B. Z. Lu, Q. M. Liu, C. Y. Wang, et al., "Ultrafast Preparation of Nonequilibrium FeNi Spinels by Magnetic Induction Heating for Unprecedented Oxygen Evolution Electrocatalysis," *Research-China* 2022 (2022): 9756983, <https://doi.org/10.34133/2022/9756983>.
16. M. L. Pan, Y. Z. Tan, and J. W. Chew, "Superior Membrane Distillation by Induction Heating of 3D rGO/Nafion/Ni Foam for Water Treatment," *Journal of Membrane Science* 616 (2020): 118609, <https://doi.org/10.1016/j.memsci.2020.118609>.
17. S. K. Sarkar, K. K. Raul, S. S. Pradhan, S. Basu, and A. Nayak, "Magnetic Properties of Graphite Oxide and Reduced Graphene Oxide," *Physica E: Low-Dimensional Systems and Nanostructures* 64 (2014): 78–82, <https://doi.org/10.1016/j.physe.2014.07.014>.
18. K. Spilarewicz-Stanek, A. Kisielewska, J. Ginter, K. Baluszynska, and I. Piwonski, "Elucidation of the Function of Oxygen Moieties on Graphene Oxide and Reduced Graphene Oxide in the Nucleation and Growth of Silver Nanoparticles," *RSC Advances* 6 (2016): 60056–60067, <https://doi.org/10.1039/C6RA10483E>.
19. B. V. L'vov, "Mechanism of Carbothermal Reduction of Iron, Cobalt, Nickel and Copper Oxides," *Thermochimica Acta* 360 (2000): 109–120, [https://doi.org/10.1016/S0040-6031\(00\)00540-2](https://doi.org/10.1016/S0040-6031(00)00540-2).
20. Y. Y. Song, T. He, Y. L. Zhang, et al., "Cobalt Single Atom Sites in Carbon Aerogels for Ultrasensitive Enzyme-free Electrochemical Detection of Glucose," *Journal of Electroanalytical Chemistry* 906 (2022): 116024, <https://doi.org/10.1016/j.jelechem.2022.116024>.
21. T. He, Y. Peng, Q. X. Jia, et al., "Nanocomposites Based on Ruthenium Nanoparticles Supported on Cobalt and Nitrogen-Codoped Graphene Nanosheets as Bifunctional Catalysts for Electrochemical Water Splitting," *ACS Applied Materials & Interfaces* 11 (2019): 46912–46919, <https://doi.org/10.1021/acsami.9b17056>.
22. X.-L. Huang, R.-Z. Wang, D. Xu, et al., "Homogeneous CoO on Graphene for Binder-Free and Ultralong-Life Lithium Ion Batteries," *Advanced Functional Materials* 23 (2013): 4345–4353.
23. A. V. Ravindra, B. Behera, and P. Padhan, "Laser Induced Structural Phase Transformation of Cobalt Oxides Nanostructures," *Journal of Nanoscience and Nanotechnology* 14 (2014): 5591–5595, <https://doi.org/10.1166/jnn.2014.9023>.
24. M. W. Kanan and D. G. Nocera, "In Situ Formation of an Oxygen-Evolving Catalyst in Neutral Water Containing Phosphate and Co<sup>2+</sup>," *Science* 321 (2008): 1072–1075, <https://doi.org/10.1126/science.1162018>.
25. C. C. L. McCrory, S. Jung, I. M. Ferrer, S. M. Chatman, J. C. Peters, and T. F. Jaramillo, "Benchmarking Hydrogen Evolving Reaction and Oxygen Evolving Reaction Electrocatalysts for Solar Water Splitting Devices," *Journal of the American Chemical Society* 137 (2015): 4347–4357, <https://doi.org/10.1021/ja510442p>.
26. Q. Q. Zha, M. X. Li, Z. H. Liu, and Y. H. Ni, "Hierarchical Co,Fe-MOF-74/Co/Carbon Cloth Hybrid Electrode: Simple Construction and Enhanced Catalytic Performance in Full Water Splitting," *ACS Sustainable Chemistry & Engineering* 8 (2020): 12025–12035, <https://doi.org/10.1021/acssuschemeng.0c02993>.
27. J. W. Ye, B. Yuan, W. L. Peng, J. X. Liang, Q. Y. Han, and R. Z. Hu, "Highly Stable Mo-NiO@NiFe-Layered Double Hydroxide Heterojunction Anode Catalyst for Alkaline Electrolyzers with Porous Membrane," *ACS Applied Materials & Interfaces* 16 (2024): 23189–23198.
28. Z. F. Liu, "Many-Body Effects at Heterogeneous Interfaces from First-Principles: Progress, Challenges, and Opportunities," *American Chemical Society Nano* 19 (2025): 5861–5870, <https://doi.org/10.1021/acsnano.4c18268>.
29. T. E. Jones, D. Teschner, and S. Piccinin, "Toward Realistic Models of the Electrocatalytic Oxygen Evolution Reaction," *Chemical Reviews* 124 (2024): 9136–9223, <https://doi.org/10.1021/acs.chemrev.4c00171>.
30. C. Han, Y. Lv, X. Tang, et al., "Phase Equilibrium Regulation in ZIF-67-Derived Electrocatalysts: Degradation Mechanism and Stability Enhancement for Oxygen Evolution Reaction," *Nano Letters* 25 (2025): 11484–11491, <https://doi.org/10.1021/acs.nanolett.5c02869>.
31. D. Xu, S.-N. Zhang, J.-S. Chen, and X.-H. Li, "Design of the Synergistic Rectifying Interfaces in Mott-Schottky Catalysts," *Chemical Reviews* 123 (2023): 1–30, <https://doi.org/10.1021/acs.chemrev.2c00426>.
32. Y. T. Wu, F. H. Wang, N. W. Ke, et al., "Self-Supported Cobalt/Cobalt Selenide Heterojunction for Highly Efficient Overall Water Splitting," *Journal of Alloys and Compounds* 925 (2022): 166683, <https://doi.org/10.1016/j.jallcom.2022.166683>.
33. C. Chatzichristodoulou, F. Allebrod, and M. B. Mogensen, "High Temperature Alkaline Electrolysis Cells with Metal Foam Based Gas Diffusion Electrodes," *Journal of The Electrochemical Society* 163 (2016): F3036–F3040, <https://doi.org/10.1149/2.005161jes>.
34. D. C. Marcano, D. V. Kosynkin, J. M. Berlin, et al., "Improved Synthesis of Graphene Oxide," *ACS Nano* 4 (2010): 4806–4814, <https://doi.org/10.1021/nn1006368>.

### Supporting Information

Additional supporting information can be found online in the Supporting Information section.

**Supporting File:** asia70647-sup-0001-SuppMat.pdf